https://doi.org/10.1016/j.engstruct.2022.115254

To Engineering Structures

Vibration-based FRP debonding detection using a Q-learning evolutionary algorithm

Zhenghao Ding, Lingfang Li*, Xiaoyou Wang, Tao Yu and Yong Xia

Department of Civil and Environmental Engineering,

The Hong Kong Polytechnic University, Kowloon, Hong Kong, China

Emails: zhenghao.ding@polyu.edu.hk; lingfang.li@connect.polyu.hk;

xiaoyou.wang@connect.polyu.hk; tao-cee.yu@polyu.edu.hk; ceyxia@polyu.edu.hk.

(* corresponding author)

Abstract

The secured bonding between the externally bonded fiber reinforced polymer (FRP) and the host structure is critical to provide the composite action of the FRP strengthened structure. Conventional FRP debonding assessment is usually based on nondestructive testing methods, which have limited sensing coverage and thus cannot detect debonding far away from the sensors. In this study, the global vibration-based method is developed to identify the debonding condition of FRP strengthened structures for the first time. An FRP strengthened cantilever steel beam was tested in the laboratory. As debonding damage is non-invertible, a series of FRP debonding scenarios were specially designed by a stepwise bonding procedure in an inverse sequence. In each scenario, the first six natural frequencies and mode shapes were extracted from the modal testing and used for detecting the simulated debonding damage via the model updating technique. An $l_{0.5}$ regularization is adopted to enforce the sparse damage detection. A new Q-learning evolutionary algorithm is developed to solve the optimization problem by integrating the K-means clustering, Jaya, and the tree seeds algorithms. The experimental results show that the debonding condition of the FRP strengthened beam can be accurately located and quantified in all debonding scenarios. The present study provides a new FRP debonding detection approach.

Keywords: FRP strengthened structures, bonding condition, Q-learning, evolutionary algorithm, vibration properties.

1. Introduction

Fiber-reinforced polymer (FRP) products are extensively applied to strengthen or retrofit the deteriorated steel and reinforce concrete (RC) structures due to their lightweight, high strength, corrosion resistance and ease of installation [1-4]. They are commonly externally bonded to the structures to improve both the strength and stiffness. The strengthening effect of the FRP products is effective only when the interface bonding is secured and reliable, while many failure modes of the FRP strengthened structures are related to debonding [2]. Therefore, many installation specifications, such as host structure surface preparation and end anchorage, were suggested to improve the interface bonding and prevent premature debonding [4]. However, FRP debonding can initiate at hot zones with bonding imperfections or stress concentration, develop along the bonding interface in an imperceptible manner, jeopardize the structural integrity and stiffness, and eventually lead to the failure of the reinforcement and even the structure. It is therefore of high significance to detect the debonding and locate the debonding zone with high accuracy.

Conventional FRP debonding detections are based on nondestructive testing (NDT) techniques [5], including strain/displacement monitoring using Fiber Bragg Grating sensing technique [6, 7] and digital image correlation technique [8, 9], acoustic emission technique [10, 11], infrared thermography technique [12, 13], microwave technique [14, 15], guided wave technique [16-18], electromechanical impedance technique [19, 20], etc. These techniques belong to a category of local identification techniques, which indicates that they can only detect the condition in the vicinity of the sensors. Therefore, they are suitable to evaluate small-scale structures only. For a practical large-scale structure, either a large number of sensors are required to fully cover the entire structure, or the damage location of the target structure is known *a priori* so that the sensors can be installed in these locations. However, the FRP debonding damage may initiate at any bonding imperfections, and thus the debonding locations are difficult to know in advance.

Compared with these local NDT techniques, the vibration-based methods evaluate the

structural health condition through analyzing the global vibration properties of the structure, for example, natural frequencies, mode shapes, mode shape curvature and frequency response function in the frequency domain [21, 22] or the time-domain responses [23, 24]. As these global vibration properties are related to the global condition, the sensors are not necessary to be installed in the vicinity of the damaged area/components. In fact, the frequency measurement can be quickly obtained with a few even one single sensors. The vibration-based technique has been studied and developed to detect damage in civil engineering structures [25-27]. The detected damage types include corrosion, cracks, delamination, etc. The technique has also been applied to evaluate the stiffness degradation and restoration before and after FRP retrofitting [28-32]. These studies show that the stiffness variation due to FRP retrofitting ranges from 16.6% to 22.2%. However, to the best knowledge of the authors, the vibration-based methods have not been applied to detect the FRP debonding damage.

Mathematically, vibration-based methods can be considered as an optimization process to update a structural model so that its predicted vibrational properties are close to the measured ones in an optimal manner [33-38]. However, these methods usually require a good initial guess of the parameters and the function gradient. In addition, identifying damage in large-scale structures is difficult when only limited measurement data are available.

Owing to the rapid development in computer technologies over the last decades, evolutionary algorithms have become increasingly popular in solving optimization problems. In particular, genetic algorithms [39], differential evolution [40], particle swarm optimizer [41], artificial bee colony algorithm [42], and tree seeds algorithm (TSA) [43] have gained great attention and recognition in the field of vibration-based damage identification. Following regulations simulated from nature, these algorithms do not require good initial conditions and gradient information. They identify an “optimal” solution in a search space in an iterative manner [44]. For instance, Maity and Tripathy [39] applied the genetic algorithm to identify structural damage based on changes in

natural frequencies. Seyedpoor and Montazer [40] proposed a two-stage method for structural damage detection using differential evolution. Kang et al. [41] improved the particle swarm optimizer by introducing an artificial immune mechanism. Sun et al. [42] constructed a nonlinear factor into the artificial bee colony algorithm to enhance its optimization performance and then applied the modified algorithm to identify linear and nonlinear system parameters. Ding et al. [43] showed that the TSA performed well in damage detection with and without considering model and measurement uncertainties. All these algorithms have generally achieved satisfactory results in tackling the multi-modal optimization problem in structural damage detection or system identification.

In view of the advantage of vibration-based damage detection techniques over NDT techniques in terms of sensing coverage and sensor number requirement, as well as the excellent performance of the evolutionary algorithm, the global vibration-based method and evolutionary algorithms are combined together in this study to identify the FRP debonding condition. Although the FRP has been used to strengthen both the metallic and RC structures, the debonding in the FRP strengthened steel structure is investigated in the current study, as a preliminary endeavour to apply the vibration-based technique to detect the FRP debonding damage. This is because the FRP debonding process is a complex and nonlinear process, especially in the RC structures [45-47], where the concrete crack and debonding typically occur simultaneously.

In this paper, a multi-sample objective function is established by minimizing the discrepancies between the measured first several modal data and those obtained from the finite element (FE) model. Two major improvements are proposed in the study. First, a sparse regularization technique [48-50] is introduced to enforce the damage identification results to several elements, which is consistent with the fact that the debonding damage may occur at a few locations only. Therefore, the identified damage results will be more accurate than the conventional regularization technique. Second, a novel integrated evolutionary algorithmic framework is proposed to minimize the objective function. The K-means clustering, Jaya, and tress seeds algorithms are used to formulate a search

strategy pool, and the individuals in the colony space can adaptively choose the most suitable search strategy in each iteration under the guidance of Q-learning [51, 52]. Such unique and novel search mechanism improves the search capacity of the method during the optimization and thus leads to more accurate debonding detection results.

2. Basic formulations of FRP debonding detection

2.1. Influence on structural rigidity of FRP bonding condition

A beam shown in Fig. 1 is used to quantify the strengthening and debonding of FRP in a beam. The initial beam has a cross−section of $h_1 \times b$ and a bending stiffness of $E_1 I_1 = E_1 b h_1^3 / 12$, where h_1 and b are the cross section height and width, respectively; $E_1 I_1$ is the flexural rigidity with E_1 being the Young's modulus of the material and I_1 being the moment of inertia. After being strengthened by a layer of FRP (tensional modulus E_2 and thickness h_2 and the same width b) as shown in Fig. 1(b), the cross-sectional area increases to $b(h_1 + h_2)$, and the neutral axis moves from the middle plane ($h_1/2$) to y_c measuring from the bottom of the beam cross section as shown in the figure. Consequently, the flexural rigidity of the composite section increases to

$$K = E_1 I_1 + E_2 I_2 + E_1 b h_1 \left(h_1/2 - y_c\right)^2 + E_2 b h_2 \left(h_1 + h_2/2 - y_c\right)^2 \tag{1}$$

where the last two terms on the right-hand side are due to the bonding effect. By contrast, if debonding occurs, the cross-section will remain the same, but the flexural rigidity will reduce to $K_d = E_1 I_1 + E_2 I_2$, which equals to the summation of the bending stiffnesses of the original structure and the FRP layer. Therefore, a stiffness reduction factor (SRF) of the cross−section can be quantified as

$$\alpha = 1 - \frac{K_d}{K} = 1 - \frac{E_1 I_1 + E_2 I_2}{E_1 I_1 + E_2 I_2 + E_1 b h_1 \left(h_1/2 - y_c\right)^2 + E_2 b h_2 \left(h_1 + h_2/2 - y_c\right)^2} \tag{2}$$

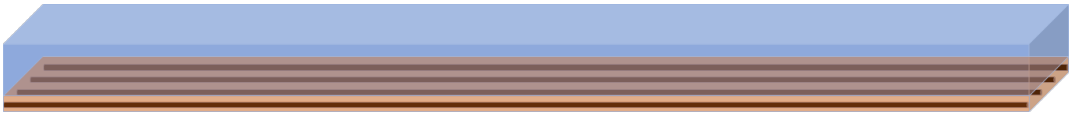

(a) Schematic diagram of FRP strengthened beam

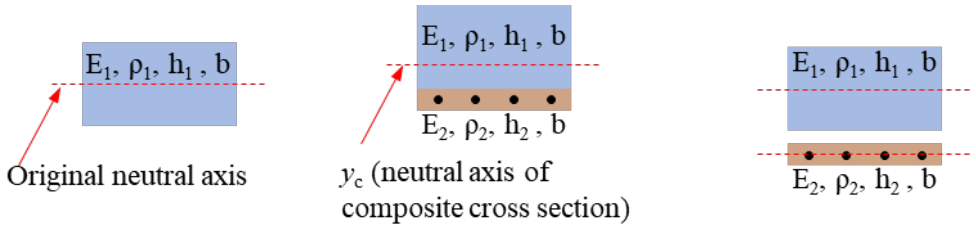

(b) Original cross−section (c) Strengthened cross−section (d) Debonded cross−section

Fig. 1 Different states of FRP strengthening in a beam structure

Both the introduction of the externally bonded FRP layer and debonding of the FRP layer have obvious influence on the structural stiffness. For example, according to Eq. (1), applying 1 mm thick FRP with tensile modulus 80 GPa to a 5 mm thick steel beam [from Fig. 1(b) to Fig. 1(c)] will increase the bending stiffness of the composite beam by 32%, while the debonding [from Fig. 1(c) to Fig. 1(d)] will reduce it by 24%. Therefore, the FRP bonding/debonding condition have a significant effect on the structural stiffness of FRP strengthened structures.

Then the FE model of the FRP strengthened structure can be established to conduct the model updating and debonding detection. As the mass loss during the debonding is negligible, only the change in the stiffness is considered in the model updating. Assuming that the structure consists of *ne* elements, its stiffness matrix in the intact state can be established as

$$\boldsymbol{K}_u = \sum_{i=1}^{ne} K^i \tag{3}$$

where K^i is the i^{th} element stiffness matrix in the undamaged state and $\sum_{i=1}^{ne}$ denotes the matrix assembling. If the debonding occurs, the stiffness matrix of the structure can be written as [53]

$$\boldsymbol{K}_d = \sum_{i=1}^{ne} K_d^i = \sum_{i=1}^{ne} \left(1-\alpha_i\right) K^i \tag{4}$$

where K_d^i represents the i^{th} element stiffness matrix in the damaged state. Based on the aforementioned assumption, debonding detection of the FRP strengthened structure is converted into identifying the SRF vector $\boldsymbol{\alpha}$. A non-zero item of $\boldsymbol{\alpha}$ indicates the debonding location and its value ($0 \le \alpha_i < 1$) quantifies the debonding severity.

2.2. Multi-sample-based model updating for debonding identification

As stated previously, the change in stiffness would lead to the alteration of vibration properties, such as the natural frequencies and mode shapes. These changes, or element damage can be identified through the model updating technique. The model updating technique adjusts the elemental parameters (here $\boldsymbol{\alpha}$) continuously so that the model properties match the measurement counterparts in an optimal way [54]. In this study, the multi-sample natural frequencies and mode shapes are used to formulate the objective function [55], given as

$$J\left(\boldsymbol{\alpha}\right) = \sum_{j=1}^{NS}\sum_{i=1}^{NM}\left\{\frac{\left[\omega_{ij}^E - \omega_i^A\left(\boldsymbol{\alpha}\right)\right]^2}{\sigma_i^2}\right\} + \sum_{i=1}^{NM}\left[1 - MAC_i\left(\boldsymbol{\alpha}\right)\right] + \varepsilon\left\|\boldsymbol{\alpha}\right\|_{0.5} \tag{5}$$

where ω_{ij}^E denotes the i^{th} natural frequency from the j^{th} measurement, and $\omega_i^A\left(\boldsymbol{\alpha}\right)$ is that from the analytical FE model, *NS* and *NM* represent the total number of measurement sets and the number of modes, respectively, and σ_i^2 is the variance of the i^{th} natural frequency and can be calculated as

$$\sigma_i^2 = \frac{1}{NS-1}\sum_{j=1}^{NS}\left(\omega_{ij} - \overline{\omega_i}\right)^2 \tag{6}$$

where $\overline{\omega_i}$ is the mean value of the i^{th} natural frequency. $MAC_i\left(\boldsymbol{\alpha}\right)$ is the i^{th} modal assurance criteria calculated as

$$MAC_i = \frac{\left(\left\{\phi_i^A\right\}^T \left\{\phi_i^E\right\}\right)^2}{\left\|\left\{\phi_i^A\right\}\right\|^2 \cdot \left\|\left\{\phi_i^E\right\}\right\|^2} \tag{7}$$

where ϕ_i^E and ϕ_i^A represent the i^{th} mode shapes from the measurement and the analytical FE model, respectively; "T" denotes the vector transpose. The first two terms in the right-hand side of Eq. (5) is to minimize the discrepancy between the FE model output and the extracted experimental frequency and mode shapes. The last term, $\varepsilon\|\boldsymbol{\alpha}\|_{0.5}$ is the sparsity regularization item, and ε is termed as the regularization parameter. A small ε poses a smaller penalty on the residual term, leading to an over-fitting solution. Conversely, a large ε results in a loss in the data fidelity. The discrepancy principle rule following Hou et al. [50] is used to select the optimal regularization parameter. Introducing the sparsity regularization item into the optimization is to enforce the sparsity of the solution, that is, most items of $\boldsymbol{\alpha}$ will approach zero except several elements with damage. By contrast, the conventional l_2 regularization will cause the optimization result of $\boldsymbol{\alpha}$ to be a full vector with small values, which indicates that the debonding occurs all along the interface and does not match the real situation that the damage (or debonding) exists in several elements only.

Using the multi-sample objective function may fully use the data sets and thus reduce the influence of the measurement noise. The variance σ_i^2 serves as the weight of each mode. A small variance—indicating a more accurate measurement—enjoys a higher weight in the objective function. As natural frequencies are scalars, their covariance values are relatively simple and can be conveniently calculated. By contrast, mode shapes are vectors. The calculation of their covariance matrices is time-consuming. Therefore, only the natural frequencies are multi-sampled in this study [55] for simplicity and computational efficiency.

Herein, through defining the objective function, the debonding detection problem is transformed into an optimization problem [43]. As traditional optimization techniques

may lead to local minimal solutions, a robust evolutionary algorithm is developed to minimize Eq. (5).

3. Proposed Q-learning based evolutionary methodology

3.1. Search strategy pool

Exploration and exploitation are two cornerstones that lead an evolutionary process toward optimization and/or convergence. Exploration is defined as visiting the whole new regions of a search space, while exploitation is defined as visiting those regions of a search space within the neighborhood of previously visited points [56]. A contradiction exists between the exploration and exploitation search modes. Specifically, an algorithm concentrating on exploration will greatly affect its convergence rate; while an algorithm focusing on exploitation may be trapped in the local minimum. As the FRP debonding can occur at any structural part due to either bonding imperfection or stress concentration, the non-zero items in $\boldsymbol{\alpha}$ may be located arbitrarily. The trade-off between the exploration and exploitation is important to optimize the search performance.

As different evolutionary algorithms show different optimization performances due to sundry search strategies, this study aims to balance the exploration and exploitation by introducing diverse search strategies. Here $\boldsymbol{x}_i$ is regarded as an arbitrary individual with n designed variable in the initial solution space that contains CS feasible solutions in total, and j represents an arbitrary dimension variable in the individual. In the proposed strategy pool, search strategies of three representative machine learning and evolutionary algorithms, namely, the K-means clustering algorithm [57], the Jaya algorithm [58], and the TSA [43], will be adopted.

The procedures of the K-means clustering strategy are presented as follows:

1. Randomly selecting initial clustering centers $\boldsymbol{C}_1, \boldsymbol{C}_2, \cdots, \boldsymbol{C}_k$ from the CS feasible solutions in the colony.

2. Assigning the remaining feasible solutions $\boldsymbol{x}_i$ to these clustering centers based on their minimum Euclidean distance. If and only if the distance $\left|\boldsymbol{x}_i - \boldsymbol{C}_k\right| \le \left|\boldsymbol{x}_i - \boldsymbol{C}_p\right|$ ($\boldsymbol{C}_p$ represent any other clustering centers), then $\boldsymbol{x}_i$ belongs to $\boldsymbol{C}_k$.

3. Calculating new clustering centers $\boldsymbol{C}_1', \boldsymbol{C}_2', \cdots, \boldsymbol{C}_k'$ as follows:

$$\boldsymbol{C}_k' = \frac{1}{N_{in}} \sum_{\boldsymbol{x}_i \in \boldsymbol{C}_k} \boldsymbol{x}_i \tag{8}$$

where N_{in} is the number of feasible solutions within a cluster. The best newly generated clustering center is sent back to replace the old solution. Applying K-means clustering strategy is beneficial to make full use of colony information.

The search mode in the Jaya algorithm is presented in Eq. (9), in which a new candidate is created by removing the old solution towards the best $\boldsymbol{x}_{best}$ while escaping the worst one $\boldsymbol{x}_{worst}$ in the colony. Such configuration ensures this strategy's exploitation ability.

$$x_{i,j}' = x_{i,j} + rand \cdot \left(x_{best,j} - \left|x_{i,j}\right|\right) - rand \cdot \left(x_{worst,j} - \left|x_{i,j}\right|\right) \tag{9}$$

The searching manner in the TSA differs from the Jaya algorithm. Several candidates are generated from the old solution based on the following strategy [52]

$$x_{i,j}' = x_{i,j} + \left(x_{i,j} - x_{k,j}\right) \cdot rand \tag{10}$$

where $\boldsymbol{x}_k$ is another different individual in the colony. Solutions are randomly created, the best one among them will be used as the final candidate. Such configuration ensures this strategy's exploration ability.

In summary, the K-means clustering strategy is beneficial to make full use of colony information; the Jaya algorithm ensures its exploitation ability; and the TSA ensures its exploration ability. The Q-learning framework [51, 52] will integrate the three algorithms to guide the individuals adaptively choose the most reasonable and suitable search strategy in each iteration, enabling the trade-off between the exploitation and exploration.

3.2. Q-learning

Q-learning is one of the most important breakthroughs in reinforcement learning, in which an intelligent agent reacts to the change in the state of the environment according to received immediate rewards or punishments. The main components of Q-learning contain an intelligent agent, an environment, states, actions, and rewards [51, 52]. In each iteration, the agent analyzes each given action in gaining future rewards or penalties and is prone to those with the maximum rewards (Q-values). In mathematics, Q-learning contains a series of states $S=\{s_1,s_2,\cdots,s_n\}$ and their corresponding actions $A=\{a_1,a_2,\cdots,a_n\}$ to be calculated. The actions are assessed in each iteration based on the following equation [52]

$$Q^{new}(s_t,a_t)=(1-\beta)Q(s_t,a_t)+\beta\left[r(s_t,a_t)+\gamma\cdot\max Q(s_{t+1},a_t)\right] \tag{11}$$

where $Q^{new}(s_t,a_t)$ and $Q(s_t,a_t)$ represent the updated and previous Q-values, respectively; β is the step size; $r(s_t,a_t)$ stands for the observed reward; γ is a discount factor and is responsible for penalizing the future reward, usually set as 0.8 [51, 52]; and $\max Q(s_{t+1},a_t)$ means the maximum Q-value for all actions. $Q(s_t,a_t)$ is compiled in a so-called Q-table. The hyperparameter β is normally set to a high value at the beginning and is reduced with iterations, thereby can be expressed as follows [51, 52]

$$\beta_t=1-\frac{0.9t}{Max_{iter}} \tag{12}$$

where t is the current iteration number and Max_{iter} is the maximum number of iterations. To select the best action, the agent ought to obey a policy $\pi: S\rightarrow A$ that maps a state S to the best action A. Fig. 2 demonstrates the calculation procedures of the Q-learning algorithm. The proposed algorithm integrates the strategy pool and the Q-learning together to compose a novel and efficient algorithm. The details of the algorithm are demonstrated in the following section.

Algorithm 1 Main steps of Q-learning algorithm

If (terminal conditions are not satisfied) **then**

1. **For** each state $s_t \in A = \{s_1, s_2, \cdots, s_n\}$ and action $a_t \in A = \{a_1, a_2, \cdots, a_n\}$;
2. Set $Q(s_t, a_t) = rand$ in the Q-table;
3. **End For**
4. Randomly choose an initial state s_t;
5. **Repeat**
6. Select the best action a_t for the current state s_t from the Q-table;
7. Perform action a_t and update the immediate reward r;
8. Obtain the maximum Q-value for the next state s_{t+1};
9. Update the Q-table entry using Eq. (11);
10. Update the current state s_t using the action corresponding with the maximum Q-value;
11. **Until** the maximum iteration number Max_{iter} reached.

End If

Fig. 2 Algorithmic structure of the Q-learning algorithm

3.3. Procedure of the Q-learning-based evolutionary algorithm

The proposed search strategy pool is combined with the Q-learning framework. Specifically, the individuals in the colony are regarded as the intelligent agents; the environment is featured by the search space of individuals; the states denote the current operation of everyone, i.e., K-means clustering strategy, search mode of the Jaya, and search mode of the TSA. The action can be defined as it changes from one state to the other. Q-learning adaptively switches the individual from one operation (state) to the other on the basis of the individual's achievement. Positive and negative rewards are given to well-performed and non-well-performed individuals in the colony.

The interaction between Q-learning and the search strategy pool can be summarized in the following three procedures [52]:

(1) Acquire the best operation to be performed according to the Q-table value for the current individual.

(2) Execute the chosen operation and compute the objective function. The immediate reward is computed as

$$r(s_t, a_t) = \begin{cases} 1 & \text{if obj improved} \\ -1 & \text{otherwise} \end{cases} \tag{13}$$

(3) Update the Q-table for the current individual using Eq. (11).

The optimization process is implemented in three phases. First, an initial colony containing CS individuals is randomly generated by

$$x_{i,j} = x_{i,j}^{l} + rand \cdot \left(x_{i,j}^{u} - x_{i,j}^{l} \right) \tag{14}$$

where $x_{i,j}^{u}$ and $x_{i,j}^{l}$ denote the upper and lower bound of $x_{i,j}$, respectively. Second, a 3×3 matrix is randomly generated as the initial Q-table for each individual in the colony. In each matrix, its rows and columns correspond the three search strategies. The individual chooses which strategy to update according to the location of the maximum Q-value in its Q-table. Subsequently, the Q-table is updated according to whether the solution improved or not. The process is repeated until Max_{iter} is reached. The pseudo-code of the proposed algorithm is outlined in Fig. 3. The algorithm keeps a simple algorithmic structure and is easy to operate as there are no special controlling parameters are introduced.

Algorithm 2 Main steps of the Q-learning-based evolutionary algorithm

%% Set the control parameters for the proposed algorithm.
%% CS : colony size; Max_{iter} : maximum iteration number.
%% $x_{i,j}^{u}$: upper bound of the $x_{i,j}$; $x_{i,j}^{l}$: lower bound of the $x_{i,j}$.
%% D : Dimension number of the problems to be optimized.
If (terminal conditions are not satisfied) **then**
1. **%% Initialization**
2. **For** $i = 1 : CS$
3. Randomly generate a 3×3 matrix as the initial Q-table.
4. **For** $j = 1 : D$
5. Generate $x_{i,j}$ by Eq. (14);
6. **End For**
7. **End For**
8. **%% Individuals' updating in the colony**
9. **Repeat** $Cycle$ =1
10. **Do** for every individual, $\boldsymbol{x}_i$
11. Select the best action, a_t for the current state s_t from the Q-table.
12. **Switch** action

13. **Case** 1
14. Update $\boldsymbol{x}_i'$ by the K-means clustering strategy;
15. **Case** 2
16. Update $\boldsymbol{x}_i'$ by Eq. (9);
17. **Case** 3
18. Determine the number of candidates $N \in [2, 0.1CS)$ randomly;
19. Update candidates by Eq. (10);
20. Update $\boldsymbol{x}_i'$ by keeping the best candidate;
21. **%% Greedy selection mechanism**
22. Evaluate $\boldsymbol{x}'$
23. **For** $i = 1 : CS$
24. **If** $\boldsymbol{x}_i'$ is superior to $\boldsymbol{x}_i$
25. **Then** $\boldsymbol{x}_i'$ is survived to the next cycle;
26. **End If**
27. Update the immediate reward based on Eq. (13);
28. Update the Q-table entry using Eq. (11);
29. Update the current state;
30. $Cycle = Cycle + 1$;
31. **Until** $Cycle = Max_{iter}$;
32. **Return** best $\boldsymbol{x}_{best}$;

End If

Fig. 3 Pseudo code of the proposed algorithm.

3.4. Benchmark verification

One representative benchmark test, named Sum-square, is used to evaluate the superiority of the proposed algorithm over other two related evolutionary algorithms, i.e., Clustering-based TSA [43] and Clustering-based Jaya algorithm [55]. The Sum-square, shown in Fig. 4, is a continuous, convex, and unimodal function, which has been widely used to test an algorithm's convergence performance. Its expression is given as follows

$$F_1(x_1, x_2, \cdots, x_D) = \sum_{i=1}^{D} i x_i^2 \quad (-100 < x_i < 100, D = 100) \tag{15}$$

The initial colony $CS = 100$ and the terminal condition is $Max_{iter} = 500$. Fig. 5(a) shows the iteration process of objective function values based on the three algorithms. The proposed Q-learning-based evolutionary algorithm can yield the largest improvements in the convergence rate and identification accuracy. Furthermore, Fig. 5(b) shows the selection proportion for the three search strategies, in which the proportions

fluctuate in the early stage and maintain a stable status after 12 iterations. This indicates that the individuals in the colony are adaptively choosing the most suitable search strategies. Moreover, although the same search strategies are adopted in other two algorithms, they suffer slow convergence. The comparisons demonstrate the necessity of introducing the Q-learning framework and the importance of maintaining an evolutionary algorithm's exploration and exploitation.

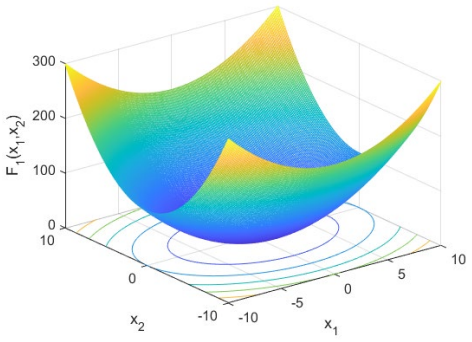

Fig. 4 Sum-square function graph

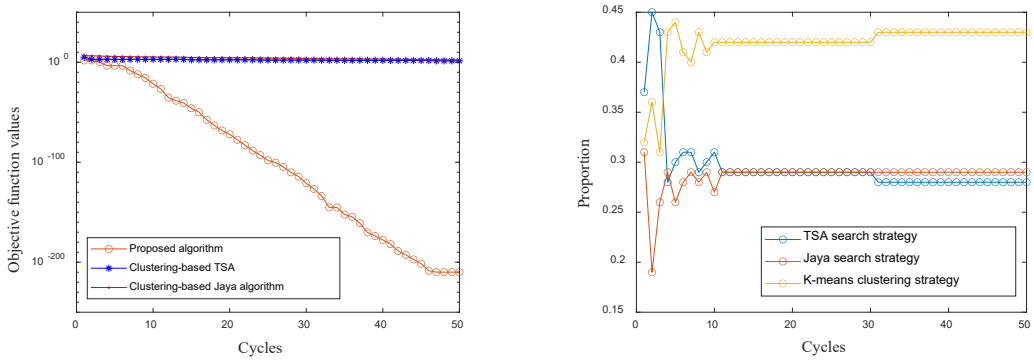

(a) (b)

Fig. 5 Optimization process of the Sum-square function

Five more mathematical benchmarks (Fig. 6) are used to verify the proposed algorithm's capacity in solving optimization problems. These functions consist of two unimodal functions (denoted by F_2 and F_3) and three multimodal functions (denoted by F_4, F_5, and F_6). The former has only one global optimal solution and is used to inspect the local search ability of the algorithm. The latter, with multiple local optimal solutions, is

employed to test the global search ability of the algorithm [56]. The mathematical formulae, dimension, search ranges, global optimal value, and the acceptance threshold of each function are presented in Table 1. When the objective function value of the best solution in a run is less than the specified threshold value, the run is treated as a successful run.

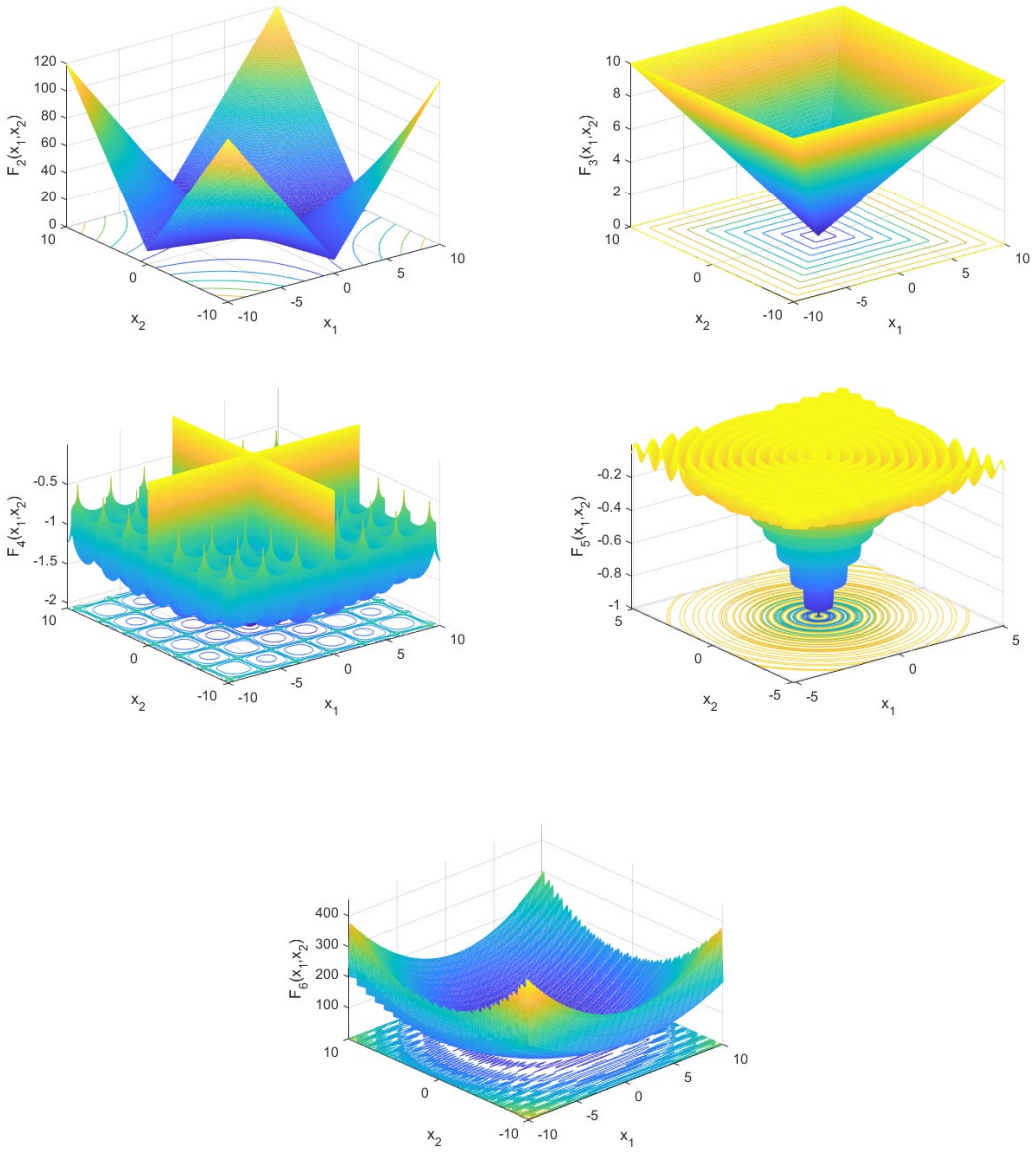

Fig. 6 The graphics of five benchmark functions.

Table 1 Formulae of all six benchmark functions.

Number	Mathematical formulae	Dimension	Range	Global solution	Acceptance threshold

F_1	$F_1(\boldsymbol{x})=\sum_{i=1}^{D} ix_i^2$	100	[–100,100]	0	10^{-8}
F_2	$F_2(\boldsymbol{x})=\sum_{i=1}^{D}\lvert x_i\rvert+\prod_{i=1}^{D}\lvert x_i\rvert$	100	[–10,10]	0	10^{-8}
F_3	$F_3(\boldsymbol{x})=\max\{x_i, i\in[1,D]\}$	30	[–100,100]	0	10^{-8}
F_4	$F_4(\boldsymbol{x})=-\dfrac{\left[\left\lvert\prod_{i=1}^{D}\sin(x_i)\exp\left(\left\lvert 100-\dfrac{\sum_{i=1}^{D}\sqrt{x_i^2}}{\pi}\right\rvert\right)\right\rvert+1\right]^{0.1}}{10^4}$	2	[–10,10]	–2.06261	–2.0626
F_5	$F_5(\boldsymbol{x})=-\dfrac{\left[1+\cos\left(12\sqrt{\sum_{i=1}^{D}x_i^2}\right)\right]}{\left(0.5\sum_{i=1}^{D}x_i^2\right)}+2$	2	[–5.12,5.12]	–1	–0.999999
F_6	$F_6(\boldsymbol{x})=\sin(3\pi x_1)^2+(x_1-1)^2\left[1+\sin(3\pi x_1)^2\right]+(x_2-1)^2\left[1+\sin(2\pi x_2)^2\right]$	2	[–10,10]	0	10^{-8}

The parameters of the proposed algorithm are set as CS = 50 and Max_{iter} = 500. The performance of the algorithm is evaluated using the following three criteria: (1) the mean and standard deviation of the best objective function value, which are used to evaluate the quality or solution obtained by the proposed algorithm; (2) the average cycle (AVEN) to reach the acceptance threshold, which represents the convergence speed; and (3) the successful rate (SR%) of the 30 independent runs, which reflects the robustness or reliability of the proposed algorithm.

The final optimization results using the proposed algorithm towards the six mathematical benchmarks are presented in Table 2. The proposed algorithm can acquire satisfactory optimizations with a fast convergence speed. The 100% SR for all benchmarks demonstrates the algorithm's excellent robustness/reliability, which lays the foundation for the following FRP debonding identification.

Table 2 Optimization results of the six benchmarks based on the proposed algorithm

Function Number	Criterion 1		Criterion 2	Criterion 3
	Mean value	Standard deviation	AVEN	SR%
1	0.00e+00	0.00e+00	7	100
2	2.17e–284	0.00e+00	11	100
3	2.48e–175	0.00e+00	14	100

4	–2.06261	9.033e–16	2	100
5	–1	0.00e+00	4	100
6	1.34e-31	6.68e-47	16	100

4. An experimental study

4.1. Model description

The proposed algorithm is applied to detect the FRP debonding of an experimental FRP strengthened steel cantilever beam (Fig. 7). The left end of the beam is fixed by a set of strong steel brackets. The total length of the host steel beam is 1000 mm, and the cross−section is 50.00 × 5.00 mm^2. The Young's modulus and density of the steel are 200 GPa and 7.85×10^3 kg/m^3, respectively. The beam is strengthened by two layers of CFRP cloth through a wet-layup process. The density of the FRP layer is estimated as 1.5×10^3 kg/m^3. The resulted FRP layer is around 1 mm thick. A standard coupon test was conducted to estimate the tensile modulus of the FRP layer in view of the possible variation of its thickness and curing condition in the wet layout process. The average thickness of the coupons is 0.87 mm and the tested tensile modulus is around 100 GPa. However, the thickness of the FRP layer in the modal test is around 1mm, possibly due to more resin is used. The extra resin will reduce the modulus of the FRP layer. Therefore, the tensile modulus of the FRP layer is estimated as 80 GPa.

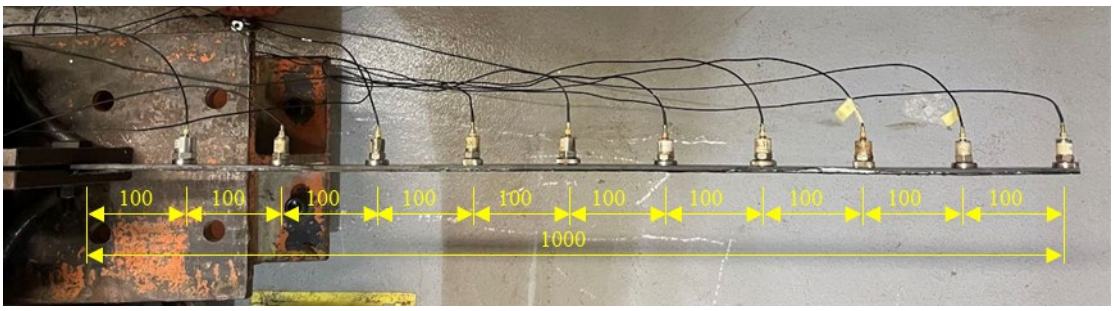

Fig. 7 Overview of the cantilever beam covered with FRP

4.2. Damage introduction and scenarios

As the debonding initiation and development are difficult to control in the loading test,

a stepwise bonding process is designed to simulate the gradual debonding process in a reversed order as shown in Fig. 8. That is, the full length FRP strip was partially bonded to the steel beam at the beginning, and three small zones were intentionally not bonded to simulate the debonding at the three positions. This state is referred to as damage/debonding scenario 3, or DS3, which has three debonded zones, namely, 1st from 0 to 50 mm, 2nd from 250 to 300 mm and 3rd from 600 to 650 mm, respectively, measuring from the fixed end to the free end. The selection of these three debonding zones may cover the high stress zone (the 1st zone) and possible bonding imperfection zones (the 2nd and 3rd zones). Subsequently, the third and second non-bonded FRP region were attached to the beam through a wet-layup process sequentially, which are referred to as DS2 and DS1, respectively. Finally, the first non-bonded region was attached, and the entire FRP strip was fully bonded, which is the intact state or DS0. The specimen of DS3 is shown in Fig. 9.

According to the calculation in Section 2, the stiffness of the debonded zone is around 24% lower than that of the bonded zone, equivalent to an SRF of 24%. Note that this is an estimated value and may be different from the real one due to the manual error in attaching the FRP strips and epoxy.

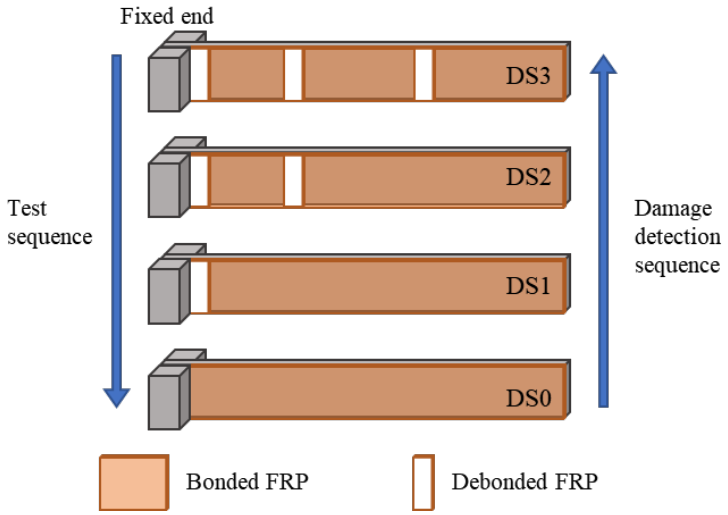

Fig. 8 Sequential FRP debonding in the cantilever beam.

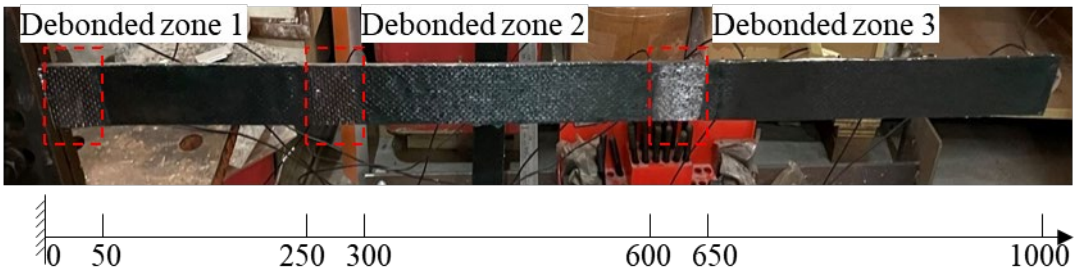

Fig. 9 Introduced debonding in the cantilever beam (DS3, Unit: mm)

4.3. Modal testing

Modal tests were conducted for each damage scenario. The beam was excited using an instrumented hammer with a rubber tip. The accelerations at 10 locations with equal spacing of 100 mm (Fig. 7) were measured by accelerometers and then collected by a datalogger (Fig. 10). The sampling frequency is 5000 Hz, and the data collection duration is 60 seconds. In each scenario, the beam was hit for 5 times and these signals were combined into a 5-minute duration signal. The input force and accelerations response of the undamaged beam are shown in Fig. 11. The frequency response functions of the beam are then calculated, and the first six frequencies and mode shapes were extracted from these stitched signals using a rational fraction polynomial method [59]. The extracted modal data of DS0 are shown in Fig. 12.

Fig. 10 Data acquisition system

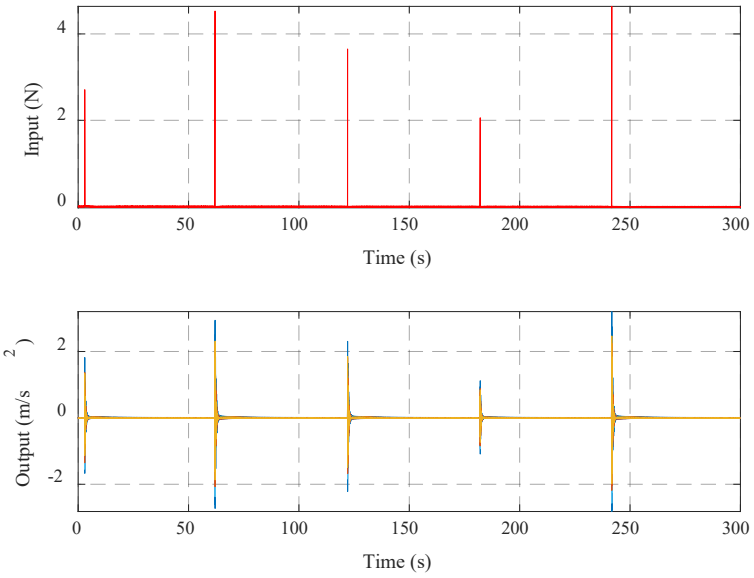

Fig. 11 Input and output time history

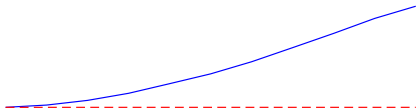

(a) Mode 1, frequency = 3.86 Hz

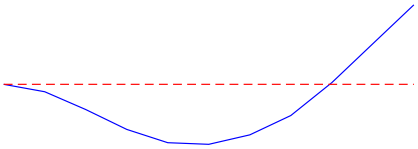

(b) Mode 2, frequency = 24.87 Hz

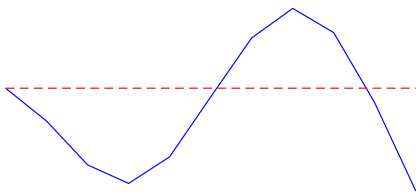

(c) Mode 3, frequency = 68.17 Hz

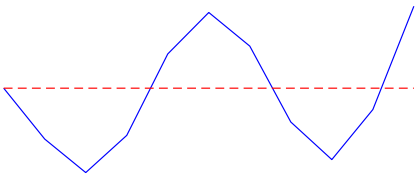

(d) Mode 4, frequency = 132.68 Hz

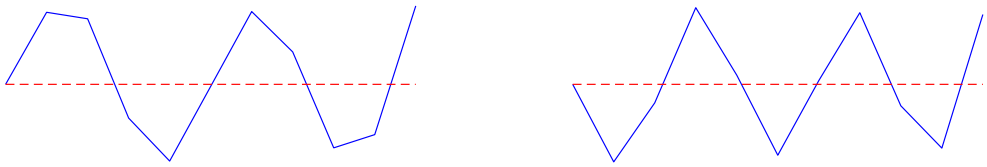

(e) Mode 5, frequency = 216.41 Hz (f) Mode 6, frequency = 318.19 Hz

Fig. 12 The measured first six mode shapes for DS0

Table 3 summarizes the first six natural frequencies and the corresponding MAC values of the experimental beam from DS0 to DS3. The natural frequencies decrease significantly from DS0 to DS1, while the changes are relatively small from DS1 to DS3. This indicates that the debonding close to the fixed end has more significant effect on the frequencies than the debonding in the mid-span. This is more apparent for the first three modes. The higher modes, namely, the 4th, 5th and 6th modes experienced a small change.

Table 3 Measured modal data of the beam in undamaged and damaged states

Mode No.	DS0 Freq. (Hz)	DS1		DS2		DS3	
		Freq. (Hz)	MAC	Freq. (Hz)	MAC	Freq. (Hz)	MAC
1	3.86	3.64 (−5.70)	99.97	3.60 (−6.74)	99.97	3.59 (−6.99)	99.96
2	24.87	23.76 (−4.46)	99.95	23.82 (−4.22)	99.96	23.55 (−5.31)	99.91
3	68.17	66.35 (−2.67)	99.90	65.70 (−3.62)	99.88	65.34 (−4.15)	99.94
4	132.68	129.73 (−2.22)	99.13	128.96 (−2.80)	99.28	128.80 (−2.92)	99.61
5	216.41	213.72 (−1.24)	99.79	213.24 (−1.46)	99.79	211.19 (−2.41)	99.83
6	318.19	315.01 (−1.00)	99.66	312.01 (−1.94)	99.60	310.76 (−2.34)	99.64

Note: Values in parentheses are relative changes (%) between DS0 and DS1 to DS3.

4.4. Damage detection

The structure is modeled using 20 Euler–Bernoulli beam elements with each being

50 mm long. In this way, each debonding zone has the same length as each element. Then the damage severity of debonding zone is equal to the reduction in the moment of inertia of the cross-section defined in Eq. (2). Therefore, the SRFs of each damaged element is assumed as 24%, and the three damage scenarios are summarized in Table 4.

Table 4 Debonding locations and extents of the experimental beam

Damage scenario	Debonding element(s)	SRF
DS1	1	$\alpha_1 = 0.24$
DS2	1,6	$\alpha_1 = \alpha_6 = 0.24$
DS3	1, 6, 13	$\alpha_1 = \alpha_6 = \alpha_{13} = 0.24$

The FE model updating is first performed to fine tune the initial FE model so that its vibration properties match the measured ones of the undamaged structure as closely as possible [58]. The first six natural frequencies and the mode shapes are used to in the model updating by applying the proposed Q-learning-based evolutionary algorithm. The flexural rigidity (*EI*) of 20 elements is chosen as the updating parameters. In the model updating, the colony size is set as $CS = 100$ and $Max_{iter} = 200$. Table 5 compares the first six natural frequencies of the initial FE model and the updated one, especially the first mode. The difference of the FE model decreases significantly after updating. The updated model can represent the real beam and will be used for debonding detection.

Table 5 Measured and analytical natural frequencies of the cantilever beam in DS0

Mode No.	Freq. (Hz)	Before updating		After updating	
		Analytical (Hz)	Difference (%)	Analytical (Hz)	Difference (%)
1	3.86	3.64	−5.70	3.79	−1.81
2	24.87	23.76	−4.46	24.55	−1.29
3	68.17	66.35	−2.67	67.68	−0.72
4	132.68	129.73	−2.22	132.49	−0.14
5	216.41	213.72	−1.24	215.88	−0.24
6	318.19	315.01	−1.00	317.23	−0.03

The damage detection is conducted from DS1 to DS3, in an inverse sequence as the experiment. The measured modal data in DS1 are used to update the fine-tuned FE model in DS0. 1% white noise is added to the measured natural frequency to generate 15 data samples. The parameters set for the Q-learning algorithm are the same as the previous model updating. The regularization parameter ε in DS1 is determined as 20 by the discrepancy principle rule following Hou et al. [50]. Due to the measurement uncertainties and the regularization term, the global optimum for the DS1 is within the neighborhood of 64.90. In addition, the C-Jaya-TSA algorithm proposed in Ref. [58] is also employed for comparison with the same algorithm operators. Although C-Jaya-TSA algorithm performed well in dealing with damage identification problems, it does not equip the adaptive selection mechanism as the proposed algorithm.

The evolutionary process of the model updating using the two algorithms is shown in Fig. 13. After around 80 cycles, the proposed algorithm converges to the neighborhood of the global optimum while the C-Jaya-TSA suffers a slow convergence. This indicates that the proposed algorithm adaptively choosing the most suitable search strategy can greatly enhance the convergence. The selection proportion of the three search strategies for this problem is shown in Fig. 14. Compared with Fig. 5(b), the three proportions fluctuate more intensely, and the TSA search strategy wins the most selection. This is

because the objective function for the damage identification is multi-modal [55] and possesses countless local optimums. Therefore, with the Q-learning framework, the search strategy focusing on exploration has more likelihood to be chosen. The objective function of the damage identification problem is more complicated than the basic mathematical benchmark problems. The algorithm may adaptively choose these search strategies more intensely to avoid the local minimum, thereby resulting in some fluctuations again after 190 cycles. Furthermore, the essence of the random search of the evolutionary algorithm would result in fluctuations to some extent in terms of the selection proportions.

The debonding identification results are shown in Fig. 15. The debonded element 1 is correctly detected using the proposed techniques, and the debonding severity (*SRF* = 0.24) is also quantified. However, several undamaged elements are falsely detected using the C-Jaya-TSA.

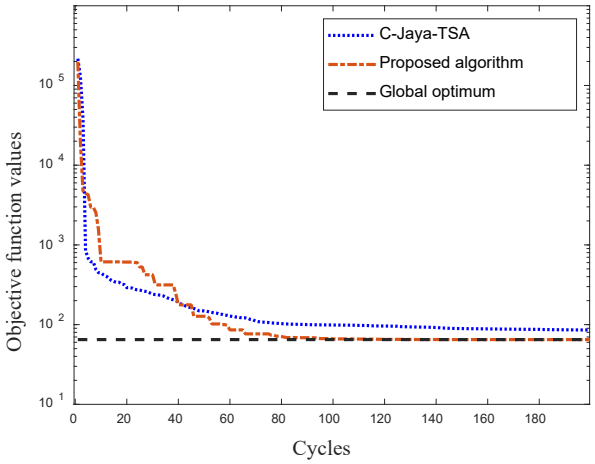

Fig. 13 Evolutionary process of the model updating for DS1

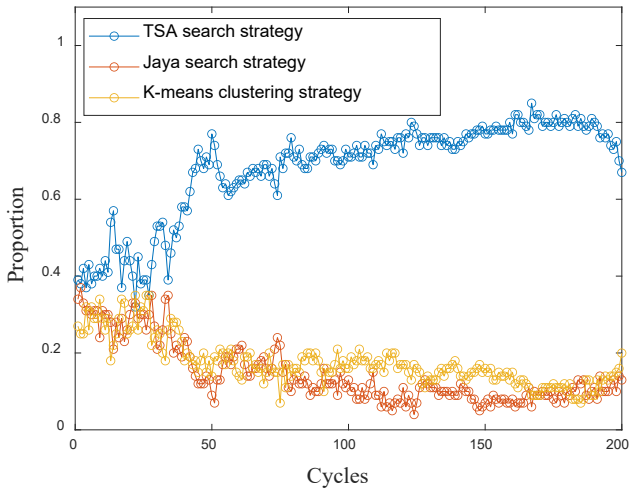

Fig. 14 Selection proportion of the three search strategies for DS1.

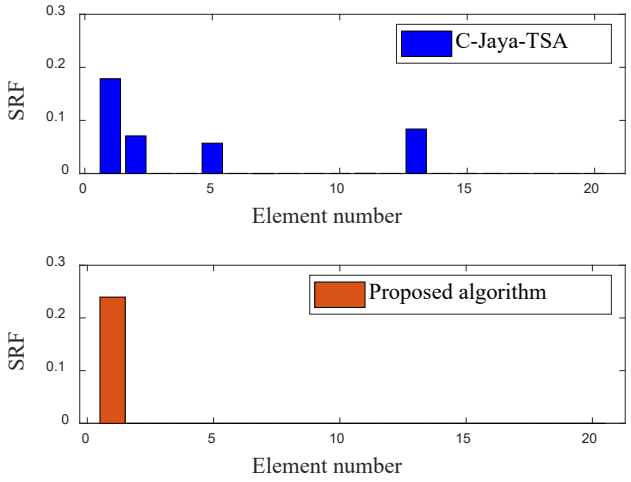

Fig. 15 Debonding identification results for DS1

The proposed technique is then applied to DS2 and DS3, in which the corresponding regularization parameters ε is set as 8 and 5, respectively. The identified results are shown in Figs. 16 and 17. In both cases, the proposed technique can detect the damage locations correctly while the C-Jaya-TSA falsely detect several intact elements. The identified SRFs of elements 6 and 13 are slightly different from the assumed value, which may be due to the measurement errors. In general, more sensors will provide more measurement data and may improve the damage identification results. The sensor location

also affects the results [60, 61]. Besides, the FRP was attached to the steel beam manually through a wet lay-up process, which may cause variations in the FRP layer thickness and epoxy quality. Consequently, the element stiffness of the strengthened beam may not be uniform. Nevertheless, the proposed algorithm can still provide satisfactory identification results.

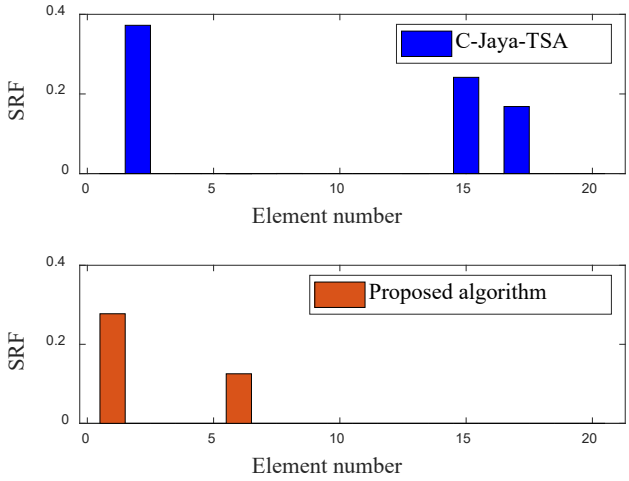

Fig. 16 Identification results for DS2

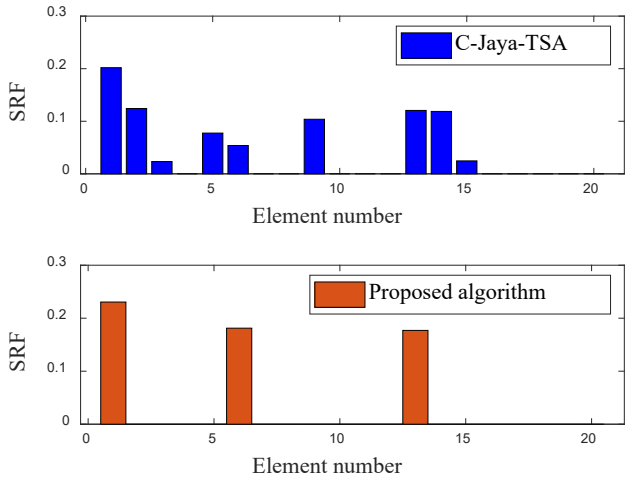

Fig. 17 Identification results for DS3

5. Conclusions and discussions

The vibration-based technique using an integrated Q-learning-based evolutionary

algorithm has been developed to detect the debonding in FRP strengthened structures for the first time. The modal data are used to formulate a multi-sample objective function with and a sparse regularization technique. A Q-learning evolutionary algorithm is proposed to solve the objective function in an optimal manner. An FRP strengthened cantilever steel beam has been tested in the laboratory and used to. The developed technique has been applied to an FRP strengthened cantilever steel beam tested in the laboratory. The following conclusions can be drawn:

1. A series of FRP debonding scenarios were designed by a stepwise bonding procedure in an inverse sequence. The FRP debonding condition is modeled as the stiffness loss of the corresponding elements, which are successfully located and quantified by the vibration-based approach via the model updating technique;
2. As the number of measurement data is less than the number of unknown parameters in the model updating, the model updating is an under-determined problem. The $l_{0.5}$ regularization technique can enforce the identification results converge to several damaged elements, overcoming the ill-posedness of the problem;
3. The developed Q-learning evolutionary algorithm can achieve the global optimization and identify the damaged element accurately.

Due to the influences of environmental factors, measurement noise, finite element modeling errors, and the complexity of identification problem, the objective function formulated in this study is complicated with many local minimums. The proposed Q-learning evolutionary algorithm integrates the characteristics and advantages of K-means clustering, Jaya, and the tree seeds algorithms. Consequently, it can adaptively choose the most suitable search strategy and effectively balance the exploration and exploitation of the algorithm, thereby enhancing its global searchability. Moreover, the Q-learning evolutionary algorithm has a simple algorithmic structure and does not introduce new controlling parameters.

The proposed method can also be used to detect poor workmanship, which is not unusual for FRP strengthening of large-scale structures, as a quality assurance measure

for FRP bonding work on site. For such uses, the bonding imperfection may be detected before the structure is heavily loaded so that the stiffness degradation is not complicated by the damage of concrete.

The strengthening of the steel structure is one application scenario of FRP, where the stiffness reduction is purely due to debonding. FRP materials are also widely used to strengthen RC structures. There are two major debonding failure modes, namely, intermediate crack induced debonding and concrete cover separation. The present algorithm may be extended for identification of intermediate crack debonding, but such extension can only be valid when it is used together with a sophisticated model that can accurately simulate the mechanism of concrete crack development associated with FRP debonding. With respect to the concrete cover separation, it leads to the stiffness loss and mass reduction, which is against the unchanged mass assumption in the algorithm. The present algorithm needs to be further developed to account for the mass change in the future.

Acknowledgement

This work is supported by the Theme-based Research Scheme project (T22-502/18-R), RGC-GRF (Project No. 15201920) and PolyU Postdoctoral Matching Fund (Project No. W18P and Project No. 1-W172).

References

[1] Teng JG, Chen JF, Smith ST, Lam L. FRP strengthened RC structures. 2002.
[2] Zhao XL, Zhang L. State-of-the-art review on FRP strengthened steel structures. Engineering Structures 2007;29:1808-23.
[3] Zhao XL. FRP-strengthened metallic structures. Crc Press; 2013.
[4] Teng JG, Yu T, Fernando D. Strengthening of steel structures with fiber-reinforced polymer composites. Journal of Constructional Steel Research 2012;78:131-43.
[5] Li DS, Zhou JL, Ou JP. Damage, nondestructive evaluation and rehabilitation of FRP composite-RC structure: A review. Construction and Building Materials 2021;271:121551.
[6] Wang H, Jiang L, Xiang P. Improving the durability of the optical fiber sensor based on strain transfer analysis. Optical Fiber Technology 2018;42:97-104.
[7] Wang H-P, Ni Y-Q, Dai J-G, Yuan M-D. Interfacial debonding detection of strengthened steel structures by using smart CFRP-FBG composites. Smart Materials and Structures 2019;28:115001.
[8] Berardi VP, Perrella M, Cricrì G. Cohesive fracture in composite systems: experimental setup and first results. Frattura ed Integrità Strutturale 2019;13:222-9.
[9] Cricrì G, Perrella M, Berardi VP. Identification of cohesive zone model parameters based on interface layer displacement field of bonded joints. Fatigue & Fracture of Engineering Materials & Structures 2022;45:821-33.
[10] Li WJ, Ho SCM, Patil D, Song GB. Acoustic emission monitoring and finite element analysis of debonding in fiber-reinforced polymer rebar reinforced concrete. Structural Health Monitoring 2017;16:674-81.
[11] Degala S, Rizzo P, Ramanathan K, Harries KA. Acoustic emission monitoring of externally bonded FRP-reinforced concrete. In: Health monitoring of structural and biological systems 2008. 2008. International Society for Optics and Photonics.
[12] Valluzzi MR, Grinzato E, Pellegrino C, Modena C. IR thermography for interface analysis of FRP laminates externally bonded to RC beams. Materials and Structures 2009;42:25-34.
[13] Lai WWL, Kou SC, Poon CS, Tsang WF, Lee K. A durability study of externally bonded FRP-concrete beams via full-field infrared thermography (IRT) and quasi-static shear test. Construction and Building Materials 2013;40:481-91.
[14] Akuthota B, Hughes D, Zoughi R, Myers J, Nanni A. Near-field microwave detection of disbond in carbon fiber reinforced polymer composites used for strengthening cement-based structures and disbond repair verification. Journal of Materials in Civil Engineering 2004;16:540-6.
[15] Navagato MD, Narayanan RM. Microwave imaging of multilayered structures using ultrawideband noise signals. NDT & E International 2019;104:19-33.
[16] Li L, Faisal Haider M, Mei H, Giurgiutiu V, Xia Y. Theoretical calculation of circular-crested Lamb wave field in single- and multi-layer isotropic plates using the normal mode expansion method. Structural Health Monitoring 2019;19:357-72.
[17] Li LF, Mei HF, Haider MF, Rizos D, Xia Y, Giurgiutiu V. Guided wave field calculation in anisotropic layered structures using normal mode expansion method. Smart Structures and

Systems 2020;26:157-74.
[18] Bastianini F, Di Tommaso A, Pascale G. Ultrasonic non-destructive assessment of bonding defects in composite structural strengthenings. Composite Structures 2001;53:463-7.
[19] Li LF, Xia Y, Chen GM. Experimental and numerical studies of debonding monitoring of FRP shear-strengthened beams using EMI technique. Journal of Aerospace Engineering 2018;31:04018048.
[20] Bhalla S, Soh CK. Electromechanical impedance modeling for adhesively bonded piezo-transducers. Journal of Intelligent Material Systems and Structures 2004;15:955-72.
[21] Chen ZW, Zhao L, Zhang J, Cai QL, Li J, Zhu SY. Damage quantification of beam structures using deflection influence line changes and sparse regularization. Advances in Structural Engineering 2021;24:1997-2010.
[22] Pappalardo CM, Guida D. System identification and experimental modal analysis of a frame structure. Engineering Letters 2018;26:56-68.
[23] Yang JN, Xia Y, Loh CH. Damage identification of bolt connections in a steel frame. Journal of Structural Engineering 2014;140:04013064.
[24] Liu K, Law SS, Xia Y, Zhu XQ. Singular spectrum analysis for enhancing the sensitivity in structural damage detection. Journal of Sound and Vibration 2014;333:392-417.
[25] Avci O, Abdeljaber O, Kiranyaz S, Hussein M, Gabbouj M, Inman DJ. A review of vibration-based damage detection in civil structures: From traditional methods to machine learning and deep learning applications. Mechanical Systems and Signal Processing 2021;147:107077.
[26] Doebling SW, Farrar CR, Prime MB, Shevitz DW. Damage identification and health monitoring of structural and mechanical systems from changes in their vibration characteristics: a literature review. 1996.
[27] Liu JL, Yu AH, Chang CM, Ren WX, Zhang J. A new physical parameter identification method for shear frame structures under limited inputs and outputs. Advances in Structural Engineering 2021;24:667-79.
[28] Baghiee N, Esfahani MR, Moslem K. Studies on damage and FRP strengthening of reinforced concrete beams by vibration monitoring. Engineering Structures 2009;31:875-93.
[29] Burgueño R, Karbhari VM, Seible F, Kolozs RT. Experimental dynamic characterization of an FRP composite bridge superstructure assembly. Composite Structures 2001;54:427-44.
[30] Bonfiglioli B, Pascale G, Martinez de Mingo S. Dynamic testing of reinforced concrete beams damaged and repaired with fiber reinforced polymer sheets. Journal of Materials in Civil Engineering 2004;16:400-6.
[31] Zanardo G, Hao H, Xia Y, Deeks AJ. Stiffness assessment through modal analysis of an RC slab bridge before and after strengthening. Journal of Bridge Engineering 2006;11:590-601.
[32] Shen DJ, Zeng X, Zhang JY, Zhou BZ, Wang W. Behavior of RC box beam strengthened with basalt FRP using end anchorage with grooving. Journal of Composite Materials 2019;53:3307-24.
[33] Perera R, Ruiz A, Manzano C. An evolutionary multiobjective framework for structural damage localization and quantification. Engineering Structures 2007;29:2540-50.
[34] Yang JN, Huang HW, Lin SL. Sequential non-linear least-square estimation for damage identification of structures. International Journal of Non-Linear Mechanics 2006;41:124-40.

[35] Yang JN, Lin SL, Huang HW, Zhou L. An adaptive extended Kalman filter for structural damage identification. Structural Control and Health Monitoring 2006;13:849-67.
[36] Xie ZB, Feng JC. Real-time nonlinear structural system identification via iterated unscented Kalman filter. Mechanical Systems and Signal Processing 2012;28:309-22.
[37] Pandey AK, Biswas M. Damage detection in structures using changes in flexibility. Journal of Sound and Vibration 1994;169:3-17.
[38] Shi ZY, Law SS, Zhang LM. Structural damage localization from modal strain energy change. Journal of Sound and Vibration 1998;218:825-44.
[39] Maity D, Tripathy RR. Damage assessment of structures from changes in natural frequencies using genetic algorithm. Structural Engineering Mechanics 2005;19:21-42.
[40] Seyedpoor SM, Montazer M. A two-stage damage detection method for truss structures using a modal residual vector based indicator and differential evolution algorithm. Smart Structures and Systems 2016;17:347-61.
[41] Kang F, Li JJ, Xu Q. Damage detection based on improved particle swarm optimization using vibration data. Applied Soft Computing 2012;12:2329-35.
[42] Sun H, Luş H, Betti R. Identification of structural models using a modified Artificial Bee Colony algorithm. Computers and Structures 2013;116:59-74.
[43] Ding ZH, Li J, Hao H, Lu ZR. Structural damage identification with uncertain modelling error and measurement noise by clustering based tree seeds algorithm. Engineering Structures 2019;185:301-14.
[44] Xu GY, Zhu WD, Emory BH. Experimental and numerical investigation of structural damage detection using changes in natural frequencies. Journal of Vibration and Acoustics 2007;129:686-700.
[45] Razaqpur A, Lamberti M, Ascione F. Debonding evolution in nonlinear FRP-retrofitted RC beams with cohesive interface. Composite Structures 2020;236:111858.
[46] Razaqpur A, Lamberti M, Ascione F. A nonlinear semi-analytical model for predicting debonding of FRP laminates from RC beams subjected to uniform or concentrated load. Construction and Building Materials 2020;233:117838.
[47] Perera R, Bueso-Inchausti D. A unified approach for the static and dynamic analyses of intermediate debonding in FRP-strengthened reinforced concrete beams. Composite Structures 2010;92:2728-37.
[48] Tikhonov AN. On the solution of ill-posed problems and the method of regularization. In: Doklady Akademii Nauk. 1963. Russian Academy of Sciences.
[49] Titurus B, Friswell MI. Regularization in model updating. International Journal for Numerical Methods in Engineering 2008;75:440-78.
[50] Hou RR, Xia Y, Bao YQ, Zhou XQ. Selection of regularization parameter for l1-regularized damage detection. Journal of Sound and Vibration 2018;423:141-60.
[51] Kaveh A, Dadras Eslamlou A, Rahmani P, Amirsoleimani P. Optimal sensor placement in large-scale dome trusses via Q-learning-based water strider algorithm. Structural Control and Health Monitoring 2022;22:e2949.
[52] Samma H, Lim CP, Saleh JM. A new Reinforcement Learning-based Memetic Particle Swarm Optimizer. Applied Soft Computing 2016;43:276-97.

[53] Wang XY, Hou RR, Xia Y, Zhou XQ. Laplace approximation in sparse Bayesian learning for structural damage detection. Mechanical Systems and Signal Processing 2020;140:106701.
[54] Kim JT, Park JH, Lee BJ. Vibration-based damage monitoring in model plate-girder bridges under uncertain temperature conditions. Engineering Structures 2007;29:1354-65.
[55] Ding ZH, Li J, Hao H. Structural damage identification using improved Jaya algorithm based on sparse regularization and Bayesian inference. Mechanical Systems and Signal Processing 2019;132:211-31.
[56] Črepinšek M, Liu S-H, Mernik M. Exploration and exploitation in evolutionary algorithms: A survey. ACM Computing Surveys 2013;45:1-33.
[57] Cai ZH, Gong WY, Ling CX, Zhang H. A clustering-based differential evolution for global optimization. Applied Soft Computing 2011;11:1363-79.
[58] Ding ZH, Li J, Hao H. Non-probabilistic method to consider uncertainties in structural damage identification based on Hybrid Jaya and Tree Seeds Algorithm. Engineering Structures 2020;220:110925.
[59] Richardson MH, Formenti DL. Parameter estimation from frequency response measurements using rational fraction polynomials. In: Proceedings of the 1st international modal analysis conference. 1982. Union College Schenectady, NY.
[60] Xia Y, Hao H. Measurement selection for vibration-based structural damage identification. Journal of Sound and Vibration 2000;236:89-104.
[61] Hou R, Xia Y, Xia Q, Zhou X. Genetic algorithm based optimal sensor placement for L1-regularized damage detection. Structural Control and Health Monitoring 2019;26:e2274.